

# *Analysis of a Direct-Bandgap GeSn-Based MQW Transistor Laser for Mid-Infrared Applications*

**Rikmantra Basu, Jaspinder Kaur & Ajay K. Sharma**

**Journal of Electronic Materials**

ISSN 0361-5235

Journal of Elec Materi

DOI 10.1007/s11664-019-07418-w



**Your article is protected by copyright and all rights are held exclusively by The Minerals, Metals & Materials Society. This e-offprint is for personal use only and shall not be self-archived in electronic repositories. If you wish to self-archive your article, please use the accepted manuscript version for posting on your own website. You may further deposit the accepted manuscript version in any repository, provided it is only made publicly available 12 months after official publication or later and provided acknowledgement is given to the original source of publication and a link is inserted to the published article on Springer's website. The link must be accompanied by the following text: "The final publication is available at [link.springer.com](http://link.springer.com)".**



# Analysis of a Direct-Bandgap GeSn-Based MQW Transistor Laser for Mid-Infrared Applications

RIKMANTRA BASU,<sup>1,3</sup> JASPINDER KAUR,<sup>1,4</sup> and AJAY K. SHARMA<sup>2,5</sup>

1.—Department of Electronics and Communication Engineering, National Institute of Technology Delhi, Narela, Delhi 110040, India. 2.—Department of Computer Science and Engineering, Dr. B. R. Ambedkar National Institute of Technology Jalandhar, Jalandhar, Punjab 144011, India. 3.—e-mail: rikmantrabasu@nitdelhi.ac.in. 4.—e-mail: jaspinderkaur@nitdelhi.ac.in. 5.—e-mail: drsharmaajayk@gmail.com

We propose the design and analysis of a group-IV material-based ( $\text{Ge}_{0.84}\text{Sn}_{0.16}/\text{Si}_{0.09}\text{Ge}_{0.8}\text{Sn}_{0.11}$ ) multiple quantum wells (MQW) transistor laser (TL) for mid-infrared applications. The base region incorporates  $\text{Ge}_{0.84}\text{Sn}_{0.16}/\text{Si}_{0.09}\text{Ge}_{0.8}\text{Sn}_{0.11}$  MQW structures pseudomorphically grown on silicon through GeSn virtual substrate, compatible with CMOS platforms for cost-effective integration of electronic and photonic circuits. With the introduction of a certain amount of tin ( $\alpha$ -Sn) content ( $\text{Sn} > 6\%$ ) into germanium (Ge), GeSn alloy shows direct bandgap, thereby achieving the population inversion condition. In addition, the use of MQW structures such as the active region enhances gain due to quantum-confinement effects, and better carrier utilization over its bulk counterpart. A comparison is made between the theoretical finding for the proposed  $\text{Ge}_{0.84}\text{Sn}_{0.16}$  MQW TL and the available experimental and theoretical data for currently employed InGaAs-based single quantum well (SQW) and MQW TLs. Estimated results show that a lower threshold base current of  $\sim 2.65$  mA and high modulation BW of  $\sim 53$  GHz can be achieved, which ensures the proposed GeSn-based MQW TL can be a good alternative for III–V-based TL.

**Key words:** Multiple quantum well, GeSn alloy, transistor laser, heterojunction bipolar transistor

## INTRODUCTION

Transistor Lasers (TLs) have already shown potential for use in long and short distance telecommunication networks for photonic integrated circuits.<sup>1–3</sup> To date, the preferred semiconductor materials for TLs are group III–V compounds such as InGaAs, GaAs, AlGaAs, and InGaN. Analytical and theoretical modeling and some experimental work of group III–V semiconductors based TLs have been carried out by several researchers.<sup>4–6</sup> However, group III–V semiconductors have limitations of lack of integration, high cost, highly toxic in nature, and maturity problems.<sup>7</sup>

Integration of electronic circuits on the Si platform has attained a remarkable level of success in the last few decades. Electronic–photonic integration, i.e., integration of electronic circuits and photonic circuits including lasers, detectors, modulators, waveguides, and interconnect on the same Si substrate, has been considered to be a dream project nowadays. Unfortunately, neither Si nor its alloy SiGe serves as a good photonic material due to the indirect nature of the bandgap. Recently, tin (Sn) incorporated group IV semiconductors have attracted much attention from workers.<sup>8–10</sup> GeSn alloys, both strained and unstrained, are now successfully grown on virtual substrates (VS) grown on Si platform. Under suitable strain or with Sn concentration in GeSn exceeding 6–8%, the alloy shows a direct band gap.<sup>11</sup> Another unique advantage of GeSn alloy is that it possesses less noise as

(Received February 11, 2019; accepted July 2, 2019)

compared to III–V semiconductor compounds.<sup>12</sup> A number of photonic devices, such as lasers<sup>13,14</sup> and photodetectors: both  $p-i-n$ <sup>15,16</sup> and HPTs<sup>17–19</sup> have been developed, ushering in a new era of group IV photonics.

With the realization of a direct bandgap semiconductors that can be grown on a Si platform, it is of interest to examine the possibility of a TL that uses group IV semiconductors alone and also to study the performance of such TLs. In this paper, we present a design of a  $\text{Ge}_{0.84}\text{Sn}_{0.16}/\text{Si}_{0.09}\text{Ge}_{0.8}\text{Sn}_{0.11}$  multiple quantum wells (MQW) transistor laser. The incorporation of direct bandgap GeSn QWs in the base leads to more carrier confinement as compared to bulk structure due to which the gain enhances. We first obtain analytically various characteristics of GeSn MQW-TL, such as threshold value of base current, laser light-output characteristics, and the optical modulation BW. A lower value of threshold base current and an enhanced modulation BW is achieved simultaneously in the case of group-IV material-based MQW TL. Secondly, we simulate the various characteristics such as spontaneous emission spectrum for TE mode, TE and TM optical gain, free carrier loss, potential variation, and optical intensity using TCAD simulation tool. We compare our present results with the corresponding values calculated for InGaAs/GaAs MQW TLs.<sup>6</sup> Though GeSn and InGaAs based TLs work at different wavelengths, the better performance predicted in our work is likely to stimulate further theoretical studies and to undertake growth of the structure and study of its performance experimentally.

The layered structure and energy band diagram is described in “[Device Structure of Proposed GeSn MQW TL](#)” section. The theory with relevant expressions and material parameters are discussed in “[Mathematical Modeling and Methodology](#)” section. The results along with discussion are given in “[Results and Discussion](#)” section, and finally, conclusions are drawn in “[Conclusion](#)”.

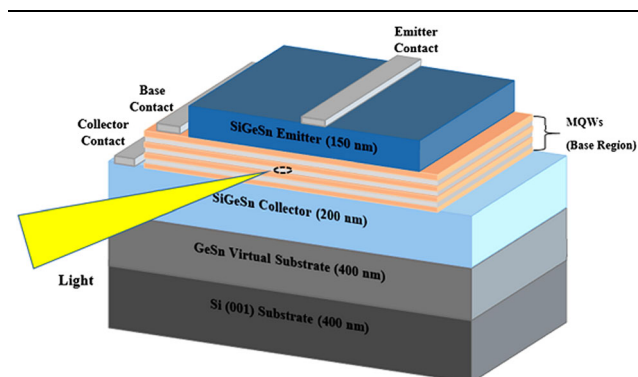


Fig. 1. Layered structure of GeSn MQW TL.

## DEVICE STRUCTURE OF PROPOSED GeSn MQW TL

Figure 1 shows the proposed 3-terminal ( $n-p-n$ )  $\text{Ge}_{0.84}\text{Sn}_{0.16}/\text{Si}_{0.09}\text{Ge}_{0.8}\text{Sn}_{0.11}$  MQW TL layered structure. A fully strain-relaxed GeSn buffer (400-nm-thick) assumed as the virtual substrate (VS) during fabrication on the silicon (001) substrate to reduce the defects and for the subsequent growth of the QWs. A thick layer of 200-nm is subsequently deposited as the collector. Three pairs of  $\text{Ge}_{0.84}\text{Sn}_{0.16}/\text{Si}_{0.09}\text{Ge}_{0.8}\text{Sn}_{0.11}$  QWs, i.e., three  $\text{Ge}_{0.84}\text{Sn}_{0.16}$  QWs and four  $\text{Si}_{0.09}\text{Ge}_{0.8}\text{Sn}_{0.11}$  barriers are then grown on a collector. The well and barrier width, respectively, are set to 16 nm and 9 nm.<sup>20</sup> Finally, the entire structure is capped by an  $n$ -type  $\text{Si}_{0.08}\text{Ge}_{0.78}\text{Sn}_{0.14}$  layer, which acts as an emitter.

The strain field of the  $i$ th layer grown on the  $\text{Ge}_{1-x}\text{Sn}_x$  buffer layer is given as

$$\epsilon_{xx}^i = \epsilon_{yy}^i = \epsilon^i = (a_0 - a_i)/a_i \quad (1)$$

$$\epsilon_{zz}^i = -2 \frac{C_{12}^{(i)}}{C_{11}^{(i)}} \epsilon^i \quad (2)$$

$$\epsilon_{xy}^i = \epsilon_{yz}^i = \epsilon_{zx}^i = 0 \quad (3)$$

where  $a_0$  denotes the lattice constant of the buffer layer,  $a_i$  is the unstrained lattice constant of the  $i$ th layer and  $C_{12}^i$  and  $C_{11}^i$  represents the elements of the stiffness matrix of the  $i$ th layer, respectively. The  $\text{Ge}_{0.84}\text{Sn}_{0.16}$  wells have a large lattice constant as compared to the buffer layer, including compressive strain in the wells. On the other side, the lattice constant of  $\text{Si}_{0.09}\text{Ge}_{0.8}\text{Sn}_{0.11}$  barriers is smaller than the buffer layer, and it leads to tensile strain for the barriers. Figure 2 shows the simulated energy band diagram using TCAD–SILVACO tool.

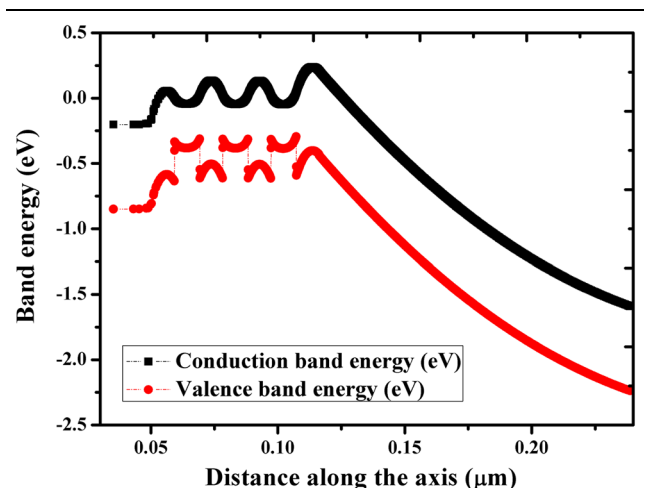


Fig. 2. Simulated energy band diagram.

## MATHEMATICAL MODELING AND METHODOLOGY

### Strained Electronic Band Structures

The linear interpolation formulae are used to obtain the most of the physical parameters for the  $\text{Ge}_{1-x}\text{Sn}_x$  and  $\text{Si}_{1-x-y}\text{Ge}_y\text{Sn}_x$  materials, except bandgaps, are defined as.<sup>21–23</sup>

$$P(\text{Ge}_{1-x}\text{Sn}_x) = (1-x)P(\text{Ge}) + xP(\text{Sn}) \quad (4)$$

$$P(\text{Si}_{1-x-y}\text{Ge}_y\text{Sn}_x) = (1-x-y)P(\text{Si}) + yP(\text{Ge}) + xP(\text{Sn}) \quad (5)$$

To obtain the bandgaps of binary or ternary alloys or compounds, the linear interpolation technique is not good due to the significant effect of bowing parameters. The unstrained bandgap energy of  $\text{Ge}_{1-x}\text{Sn}_x$  and Ge-like  $\text{Si}_{1-x-y}\text{Ge}_y\text{Sn}_x$  can be calculated from the expression given by<sup>20</sup>

$$E_g^\Gamma(\text{Ge}_{1-x}\text{Sn}_x) = (1-x)E_g^\Gamma(\text{Ge}) + xE_g^\Gamma(\text{Sn}) - b_{\Gamma}^{\text{GeSn}}x(1-x) \quad (6)$$

$$E_g^\Gamma(\text{Si}_{1-x-y}\text{Ge}_y\text{Sn}_x) = (1-x-y)E_g^\Gamma(\text{Si}) + yE_g^\Gamma(\text{Ge}) + xE_g^\Gamma(\text{Sn}) - b_{\Gamma}^{\text{SiGe}}y(1-x-y) - b_{\Gamma}^{\text{SiSn}}x(1-x-y) - b_{\Gamma}^{\text{GeSn}}xy \quad (7)$$

where  $E_g^\Gamma(\text{Ge}) = 0.7985$  eV,  $E_g^\Gamma(\text{Sn}) = -0.413$  eV and  $E_g^\Gamma(\text{Si}) = 4.185$  eV are the direct bandgap energies of Ge, Sn and Si respectively, and the bowing parameters are  $b_{\Gamma}^{\text{SiGe}} = 0.21$  eV,  $b_{\Gamma}^{\text{GeSn}} = 1.94$  eV and  $b_{\Gamma}^{\text{SiSn}} = 13.2$  eV, respectively.<sup>24</sup>

### Absorption of Free-Carriers and Confinement Factor

In electronic and photonic devices, different layers contain impurities through the doping process, and as a result, there exist a large number of free carriers in different layers or regions. These free electrons and holes cause a transition from one state (wave vector  $k$ ) to another state (wave vector  $k'$ ) in the same band by absorbing photons. The absorption of free-carriers may be significant because of heavily doped regions and can be explained by the Drude–Lorentz equation.<sup>25</sup>

$$\alpha_f = \frac{e^3 \lambda^2}{4\pi^2 c^3 \epsilon_0 N_\Gamma} \left[ \frac{N_\Gamma}{\mu_\Gamma (m_c^*)^2} + \frac{N_L}{\mu_L (m_L^*)^2} + \frac{P}{\mu_P (m_h^*)^2} \right]. \quad (8)$$

where  $N_\Gamma$ ,  $N_L$  denotes the electron densities in the conduction valleys ( $\Gamma$  and  $L$ ),  $m_c^*$ ,  $m_L^*$  indicates the effective masses of the electron in the conduction

valleys ( $\Gamma$  and  $L$ ),  $m_h^*$  is the effective mass of hole in the valence band,  $\mu_L$ ,  $\mu_\Gamma$  are the electron mobilities in the  $\Gamma$  and  $L$  conduction band,  $\mu_h$  states the hole mobility of the valence band and the free space wavelength is given by  $\lambda$ . The electron and hole mobility of germanium in the  $L$ -conduction band at room temperature is described as<sup>24</sup>

$$\mu_L = \frac{\mu_{L0}}{1 + \sqrt{N_L \times 10^{-17}}}, \mu_p = \frac{\mu_{p0}}{1 + \sqrt{P \times 2.1 \times 10^{-17}}} \quad (9)$$

where  $\mu_{L0} = 3900$   $\text{cm}^2 \text{V}^{-1} \text{s}^{-1}$ ,  $\mu_{p0} = 1900$   $\text{cm}^2 \text{V}^{-1} \text{s}^{-1}$   $N_L$  and  $P$  units is in  $\text{cm}^{-3}$ . However, the value of the electron mobility of germanium in the  $\Gamma$  conduction band is still not available in the literature. So we can summarize that (1) the absorption of free-carriers is directly proportional to  $\lambda^2$ , which is good for long-haul communication networks,<sup>24,26</sup> (2) the absorption of free-carriers is directly proportional to  $n^{3/2}$  will be significant for high doping concentration,<sup>24,27</sup> (3) the absorption of free-carriers is inversely proportional to the  $(m_h^*)^2$  indicating that it could be useful for small effective mass.

### Optical Gain Spectra

With the calculated band structures, we can calculate the optical gain spectra (TE and TM) in the GeSn base and collector fully strain-relaxed with respect to the buffer layer, taking into consideration a Lorentzian function with a linewidth of full width half maximum (FWHM),  $\Gamma$  as follows.<sup>18,19</sup>

$$g_w^{\text{TE}}(h\omega) = \frac{\pi}{n_r c \epsilon_0 L_{\text{QW}}} \left( \frac{e}{m_0} \right)^2 \left[ 1 - \exp\left( \frac{h\omega - \Delta F}{k_B T} \right) \right] \times \sum_{\sigma=L,U} \sum_{n,m} \int_0^\infty \frac{dk_t}{2\pi} k_t M_{nm}^{\sigma,\text{TE}}(k_t) \frac{f_n(k_t) [1 - f_m^\sigma(k_t)] \Gamma / 2\pi}{[E_n(k_t) - E_m^\sigma(k_t) - h\omega]^2 + (\Gamma/2\pi)^2} \quad (10)$$

$$g_w^{\text{TM}}(h\omega) = \frac{\pi}{n_r c \epsilon_0 L_{\text{QW}}} \left( \frac{e}{m_0} \right)^2 \left[ 1 - \exp\left( \frac{h\omega - \Delta F}{k_B T} \right) \right] \times \sum_{\sigma=L,U} \sum_{n,m} \int_0^\infty \frac{dk_t}{2\pi} k_t M_{nm}^{\sigma,\text{TM}}(k_t) \frac{f_n(k_t) [1 - f_m^\sigma(k_t)] \Gamma / (2\pi)}{[E_n(k_t) - E_m^\sigma(k_t) - h\omega]^2 + (\Gamma/2\pi)^2} \quad (11)$$

where  $n_r$  indicates the background refractive index,  $\epsilon_0$  is the permittivity (free space),  $c$  denotes the speed of light (in free space),  $e$  signifies the unit electronic charge,  $m_0$  is the free electron mass,  $h\omega$  is the photon energy,  $\Gamma$  denotes the full width at half

maximum of the Lorentzian line shape,  $\Delta F = F_C - F_V$  represents the quasi-fermi level separation,  $L_{\text{QW}}$  is the width of the QW and  $f_n(k_t)$  indicates the occupation number of the CB state at  $k_t$ .

For quantum wells, it is required to determine the polarization-dependent TE and TM momentum matrix element for the transverse electric and magnetic optical gain spectra. The average squared momentum matrix elements (TE polarized) are described as<sup>19</sup>

$$M_{nm}^{U,\text{TE}}(k_t) = \left[ \frac{3}{2} \langle f_n | g_m^{(1)} \rangle^2 + \frac{1}{2} \langle f_n | g_m^{(2)} \rangle^2 \right] M_b^2 \quad (12)$$

$$M_{nm}^{L,\text{TE}}(k_t) = \left[ \frac{3}{2} \langle f_n | g_m^{(4)} \rangle^2 + \frac{1}{2} \langle f_n | g_m^{(3)} \rangle^2 \right] M_b^2 \quad (13)$$

where  $f_n$  is the wavefunction of the  $n$ th electron subband in the  $\Gamma$ —conduction valley,  $g_m^{(1)}$  and  $g_m^{(2)}$  ( $g_m^{(3)}$  and  $g_m^{(4)}$ ) represents the eigen functions of the upper or lower block of the (“ $J = 4$ ”) Luttinger–Kohn Hamiltonian, and  $M_b^2 = \frac{m_0}{6} E_p$  is the moment matrix element with optical energy  $E_p$ . Similarly, average squared momentum matrix elements (TM polarized) can be calculated.

### Modal Gain, Threshold Lasing Condition and Confinement Factor

The two most important basic parameters, modal gain and threshold lasing modal gain, describe the laser performance characteristics. Modal gain defines the optical gain for the modes (guided) in a Fabry–Perot laser cavity, while the threshold modal gain signifies the required modal gain to overcome the losses (radiation + background) for coherent light emission to take place. In addition, with the use of optical confinement factor, it is possible to convert material gain to the modal gain because different modes have a capability to experience a different amount of optical gain. The general equation of the modal gain  $G_{\text{modal}}$  for a multiple quantum-wells (MQW) laser with  $N_w$  wells is described as.<sup>24</sup>

$$G_{\text{mod}} = N_w \Gamma_w^{\text{TE}} g_w^{\text{TE}}(h\omega) + N_w \Gamma_w^{\text{TM}} g_w^{\text{TM}}(h\omega) \quad (14)$$

where  $\Gamma_w^{\text{TE}}$  and  $\Gamma_w^{\text{TM}}$ , respectively, denote the optical confinement factors (TE and TM) per well of guided modes, and  $g_w^{\text{TE}}$  and  $g_w^{\text{TM}}$ , respectively, represent the material gain (TE and TM) per well. The optical confinement factors (TE and TM) per well can be expressed as

$$\Gamma_w^{\text{TE}} = \frac{\frac{n_w}{2n_0} \int_w (|E_x|^2 + |E_y|^2) dydz}{\frac{1}{2} \int_{-\infty}^{\infty} \int_{-\infty}^{\infty} \text{Re}[E \times H^*] \cdot \hat{x} dydz} \quad (15)$$

$$\Gamma_w^{\text{TM}} = \frac{\frac{n_w}{2n_0} \int_w (|E_z|^2) dydz}{\frac{1}{2} \int_{-\infty}^{\infty} \int_{-\infty}^{\infty} \text{Re}[E \times H^*] \cdot \hat{x} dydz} \quad (16)$$

where  $n_w$  represents the refractive index and  $n_0 = \sqrt{\mu_0/\epsilon_0}$  denotes the intrinsic impedance.

At the threshold lasing condition, the required modal gain for a resonant laser cavity of length  $L$  is given by

$$G_{\text{th}} = \alpha(n) + \frac{1}{2L} \ln \frac{1}{R_1 R_2} \quad (17)$$

Here,  $R_1$  and  $R_2$  indicate the reflectivity of the mirror. Once the lasing condition satisfies, modal gain reaches the threshold modal gain.

To simulate GeSn-SiGeSn MQW TL, the commercially available TCAD-Silvaco software,<sup>28</sup> from Silvaco Inc, was used. Specifically, device simulation provides a platform for better physics insights, cut down the cost of the finalized physical device, realistic predictive performance, and faster development time of device structure. The simulation program solves the current density, Poisson, and continuity equations by using a standard procedure for materials, including the Auger, and Shockley–Read–Hall recombination mechanism, and hetero-junction model. Table I indicates different parameters used in the device simulation of the proposed structure. For physical device modeling of the MQW-TL, several physical models were implemented to model the device characteristics accurately. The drift–diffusion model with Fermi–Dirac is used. This is a statistical approach to describe 2D carrier transport. For carrier generation and recombination, it utilized the different models such as Auger (AUGER), Shockley–Read–Hall (SRH), concentration-dependent SRH (CONSRH), and OPTR. We use the SPONT model for optical recombination in the well and barrier regions instead of the default optical recombination model (OPTR). By enabling FLDMOB statement, the electric-field-dependent mobility model has been used in our simulation. We use the Newton method to solve a fully coupled system of drift–diffusion and laser rate equations.<sup>29</sup>

## RESULTS AND DISCUSSION

We have achieved various characteristics of proposed  $\text{Ge}_{0.84}\text{Sn}_{0.16}$  MQW TL at 300 K by using parameter values mentioned in Table I.<sup>20</sup> The calculated values of various material parameters for  $x = 16\%$ , for base doping  $1 \times 10^{18} \text{cm}^{-3}$ , for B–E voltage ( $V_{\text{BE}} = 0.6$  to  $1 \text{V}$ ) are listed in Table II using linear interpolation formulae and some standard analytical equations.<sup>24</sup> The calculated laser characteristics are given in Table III, using the values given in Ref. 28. In this present work, most of the characteristics of the proposed GeSn MQW-TL

**Table I. Parameters of various layers of the structure**

Layer	Material	Thickness (nm)	Doping (cm <sup>-3</sup> )	Dopant	Type
Emitter	SiGeSn	150	1 × 10 <sup>19</sup>	Phosphorus	<i>n</i>
Barrier	SiGeSn	9	1 × 10 <sup>18</sup>	Boron	<i>p</i>
Well	GeSn	16	–	–	<i>i</i>
Collector	SiGeSn	200	1 × 10 <sup>17</sup>	Phosphorus	<i>n</i>
Virtual-substrate	GeSn	400	–	–	<i>i</i>
Substrate	Si	400	–	–	<i>i</i>

**Table II. Material parameters**

Parameters	Value
Energy band gap “ $E_g$ ”	0.3439 eV(GeSn), 0.64685 eV (SiGeSn)
Electron mobility “ $\mu_n$ ”	4500 (cm <sup>2</sup> /Vs)
Hole mobility “ $\mu_p$ ”	1900 (cm <sup>2</sup> /Vs)
Effective DOS in conduction band “ $N_c$ 300”	1.04 × 10 <sup>19</sup> (cm <sup>-3</sup> )
Effective DOS in valence band “ $N_v$ 300”	6.0 × 10 <sup>18</sup> (cm <sup>-3</sup> )
Carrier lifetime “ $\tau_n$ ” and “ $\tau_p$ ”	1.0 × 10 <sup>-3</sup> (s)
Radiative recombination coefficient “ $B_{\text{copt}}$ ”	6.41 × 10 <sup>-14</sup> (cm <sup>3</sup> /s)

**Table III. Laser parameters**

Laser parameters	Value
Photon energy (eV)	0.49
$N_{\text{eff}}$ (effective refractive index)	4.5
RR (reflection from the front mirror) (%)	32
RF (reflection from the rear mirror) (%)	32
Cavity length ( $\mu\text{m}$ )	100
Gain <sub>mod</sub> (modal gain for multiband k.p. model)	5
Max <sub>ch</sub> (maximum change in photon densities) (cm <sup>-1</sup> )	2.5

device structure are obtained through simulation using SILVACO tool, and some of the characteristics were obtained analytically through MATLAB. The optimum threshold value of base current, optical confinement of carriers, and laser-light power output are computed for three InGaAs and GeSn QWs placed at a position of 39 nm, 59 nm, and 79 nm from the E–B junction. The terminal currents are obtained from the continuity equation solution.<sup>30</sup> The virtual state (VS) is assumed as a path for the movement of injected charge carriers from bulk to nanostructures. Small signal modulation BW is estimated by using Statz-De Mars laser rate equations.<sup>31–33</sup>

The base threshold current is the minimum base current required for lasing action. First, the emission will be incoherent before the threshold, but after the threshold, the light emission will be coherent and will cause lasing action. So lasing to occur early base threshold current should be low as much as possible. If the base current is not able to produce light emission, the collector–base junction, which is reverse biased, will extract the carriers. This increases the switching speed of the transistor laser as compared to the diode laser. Threshold base current density is expressed with the basic transistor equation.

$$J_{\text{Bth}} = J_{\text{E}} - J_{\text{C}} \quad (18)$$

where  $J_{\text{E}}$  represents the emitter current density,  $J_{\text{C}}$  denotes the collector current density and threshold base current density is denoted by  $J_{\text{Bth}}$ .

In Fig. 3 the threshold value of base current is estimated for a GeSn and InGaAs based multiple quantum well TL structures positioned at 39 nm, 59 nm and 79 nm respectively. A comparison is made between InGaAs and GeSn based TL for different quantum well width, i.e.,  $t_{\text{qw}} = 10$  nm, 12 nm and 16 nm respectively. It appears from Fig. 3 that the threshold base current is smaller for QW that is nearer to emitter–base (EB) junction. As QW position reaches towards the BC junction, the base threshold current shows a sharp rise. This nature for the single quantum well (SQW) has already been obtained in Ref. 4. For quantum well width  $t_{\text{qw}} = 16$  nm, the value of 21.5 mA for threshold value of base current for QW positioned at 59 nm has been in good agreement with the experimental value of 22 mA. The base threshold current value of 7.06 mA and 2.65 mA, respectively, for InGaAs TL and GeSn TL with QW placed at 59 nm. As evident from Fig. 3c, the minimum threshold value of base current is obtained for GeSn TL as compared to InGaAs TL for quantum well width = 16 nm. GeSn based TL shows a lower value of threshold base current as compared to the InGaAs based TL.

The calculated threshold base currents are compared with the corresponding experimental and some of the theoretical values of currently employed

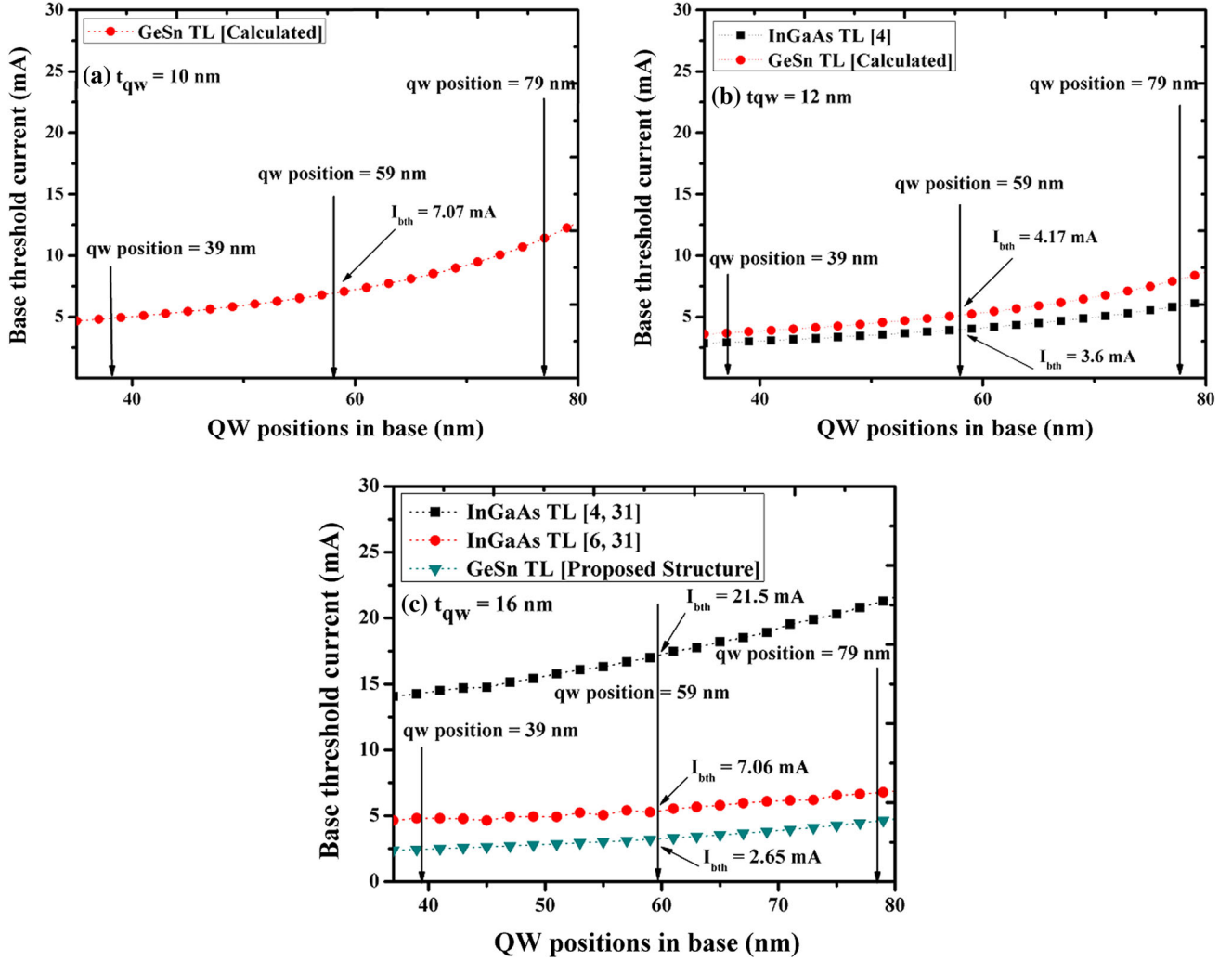


Fig. 3. Comparison of threshold base current of InGaAs and GeSn TL for different quantum well widths (a)  $t_{qw} = 10$  nm, (b)  $t_{qw} = 12$  nm, (c)  $t_{qw} = 16$  nm.

Table IV. Comparative study of the InGaAs and GeSn TL for threshold base current  $I_{bth}$  for quantum well width  $t_{qw} = 10$  nm, 12 nm and 16 nm

Multiple quantum well				Single quantum well			
GeSn TL (proposed structure)		InGaAs TL (theoretical) <sup>6</sup>		InGaAs TL (theoretical) <sup>4,28</sup>		InGaAs TL (experimental) <sup>3,34-36</sup>	
$t_{qw}$ (nm)	$I_{bth}$ (mA)	$t_{qw}$ (nm)	$I_{bth}$ (mA)	$t_{qw}$ (nm)	$I_{bth}$ (mA)	$t_{qw}$ (nm)	$I_{bth}$ (mA)
10	7.07	—	—	—	—	—	—
12	4.17	—	—	12	3.6	12	40
16	2.65	16	7.06	16	21.5	16	22

InGaAs-based single QW and MQW TL for three different quantum well widths. As shown in Table IV minimum base threshold current is obtained for the proposed GeSn-based TL for quantum well width = 16 nm as compared to InGaAs-

based TL. This is attributed to the carrier confinement and GeSn MQW inserted in the base.

Figure 4 shows the estimated values of light output power with an increasing base current for MQW-TL for two different materials InGaAs and

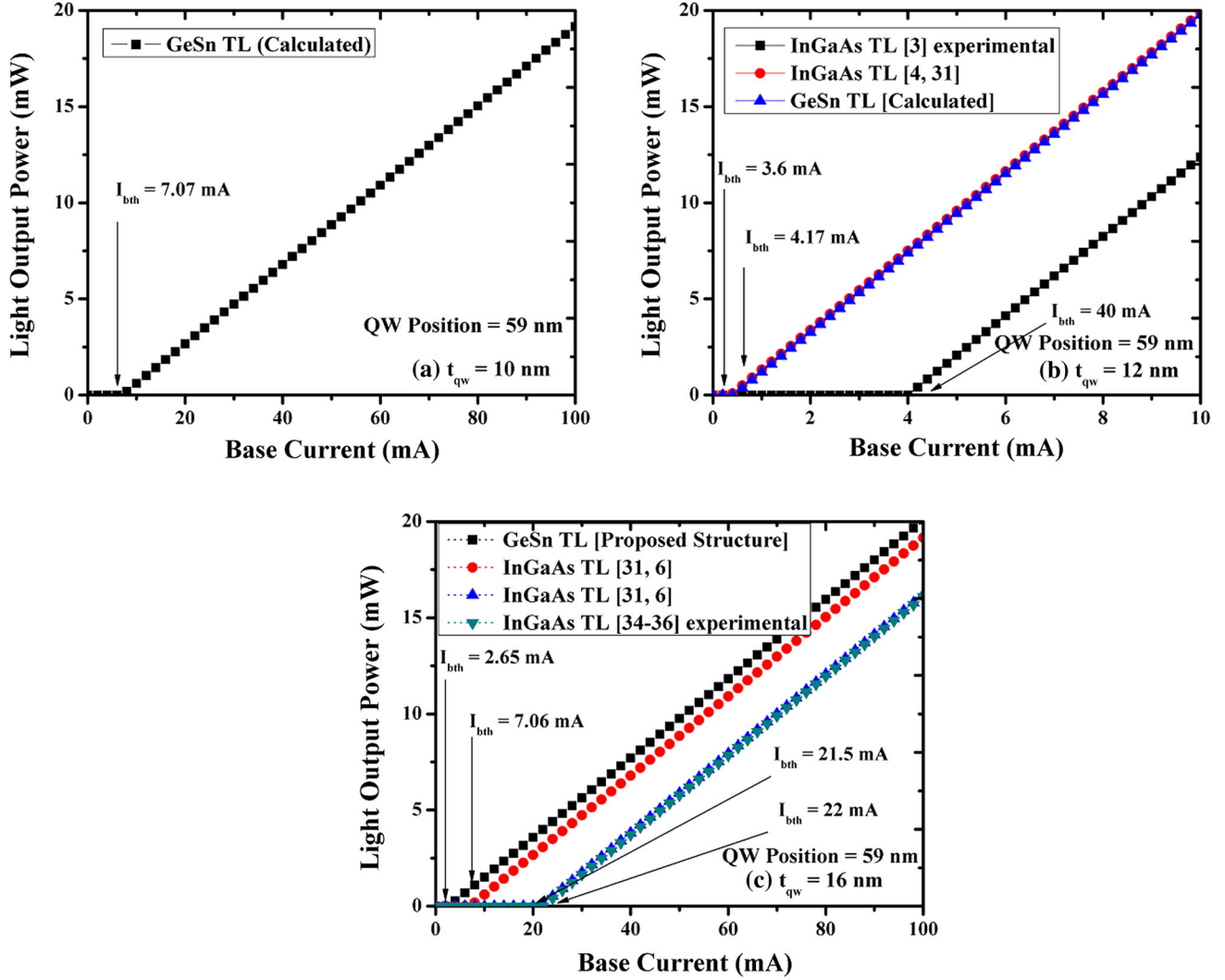


Fig. 4. Comparison of light output power a function of base current for InGaAs and GeSn based TL (QW position = 59 nm) (a)  $t_{qw} = 10$  nm, (b)  $t_{qw} = 12$  nm, (c)  $t_{qw} = 16$  nm.

GeSn at QW position 59 nm with different quantum well width ( $t_{qw} = 10$  nm, 12 nm, and 16 nm, respectively). As shown in Fig. 4, light emission occurs once the base current exceeds the threshold value. It shows the linear relation with the base current. Lesser the value of base threshold current density will cause early emission of coherent light. The minimum threshold base current is achieved for GeSn TL, and at the same time maximum light output power is obtained in this case for quantum well width  $t_{qw} = 16$  nm, as shown in Fig. 4c.

The light output power  $P$  shows linear relation with base current, above a threshold current, and the relation is given by,<sup>6,34</sup>

$$P = (\hbar\omega/q)[\alpha_m/\alpha + \alpha_m][I_b - I_{bth}] \quad (19)$$

where  $q$  denotes the unit electronic charge,  $\alpha_m$  signifies the mirror loss and,  $\hbar$  is the Planck's constant.

Figure 5 compares the small signal modulation response of InGaAs and GeSn TL. The resonance frequency and consequently the modulation BW increases substantially for GeSn material based TL as compared to InGaAs based TL. Modulation response of a TL is given by the ratio of optical output at the base to the electrical input current for the operating range of frequency. The Statz De mars laser rate equation performs the AC and DC analysis to obtain the optical modulation bandwidth. Modulation response helps in calculation of the modulation bandwidth, which also indicates the switching speed. For higher modulation bandwidth, the switching speed of the device will be higher.<sup>37</sup>

Modulation response is given by

$$H_m(\omega) = \frac{S(\omega)}{J(\omega)} \quad (20)$$

where  $S(\omega)$  indicates light output and  $J(\omega)$  indicates input current signal and  $H_m(\omega)$  indicates the modulation response of the transistor laser. It is now of interest to make a comparison of modulation bandwidth for the proposed GeSn TL and InGaAs-based TL. Table V gives the comparative data of modulation bandwidth for the quantum well width of 16 nm. The proposed GeSn TL is able to provide modulation bandwidth of  $\sim 53$  GHz, which is higher than the InGaAs-based TL. This can be explained on the basis of a threshold base current. As shown in Table V, the minimum threshold base current has been obtained for the proposed GeSn-based TL. Note that the theoretical results cannot be compared with experimental results of GeSn TL as no experimental data has yet been available in the literature for GeSn TL.

Assuming the parameters given in Table I, we calculated the base current ( $I_B$ ) and collector current ( $I_C$ ) with the variation of base-emitter voltage ( $V_{BE}$ ), the TonyPlots of which are illustrated in Fig. 6a. As this work focuses on low bias voltages,  $V_{BE}$  is increased up to 1 V, and fixed values of the collector-emitter voltage ( $V_{CE} = 2$  V) are considered. The TonyPlot shows that the base current monotonically increases, while the collector current increases sharply from  $V_{BE} = 0.4$  V. This sudden increase in collector current is due to the onset of

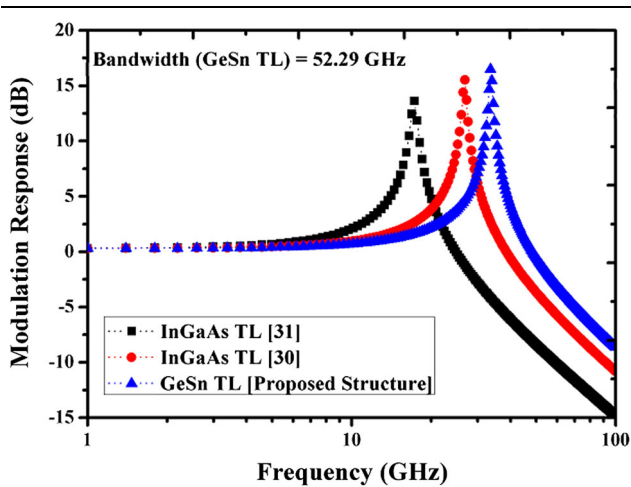


Fig. 5. Small-signal modulation response for InGaAs and GeSn TL.

lasing action from that point. Figure 6b depicts the well-confinement factor. As the base-emitter voltage ( $V_{BE}$ ) approaches 0.4 V, the confinement of carriers takes place in the wells for lasing action. Figure 6c depicts the photon density at base-emitter voltage 0.4 V. It is clearly shown that there is a sharp rise in photon density as the stimulated emission takes place at base voltage  $V_{BE} = 0.4$  V.

Figure 7 shows the electric potential variation across the distance from the emitter to the collector for different base-emitter voltage. It is evident that the electric potential through the depth (distance from the emitter to collector) of GeSn based TL increases with increasing base-emitter voltage from 0.6 V to 1.05 V.

Figure 8 shows the free carrier loss across the different layers of MQW TL at a different base-emitter voltage ( $V_{BE}$ ). It is clearly revealed that the maximum free carrier loss occurs in the emitter region and decreases through the depth of the GeSn TL structure (distance from the emitter to collector) as the base-emitter voltage increases. In actual device structures, different regions or layers doped with impurities and consequently, there exist a large number of free carriers in different regions. These free electrons and holes make a transition from one state to another state in the same band by absorbing photons. The free-carrier loss may be significant because of heavily doped regions and can be explained by Drude-Lorentz equation.<sup>24</sup>

Figure 9 indicates the TE spontaneous emission rate density with the variation of photon energy. TE and TM optical gain and the spontaneous emission spectrum are calculated in the active region of TL using the bound state energies that are fully coupled to the electrostatic potential. From Fig. 9, it is evident that the spontaneous emission spectrum is estimated above threshold as a function of photon energy. The fast-increasing TE spontaneous emission spectrum is obtained as the TE gain reaches the lasing threshold condition. The spontaneous emission spectrum is peaked around 0.59 eV (emission wavelength = 2.883  $\mu\text{m}$ ). Hence,  $\text{Ge}_{0.84}\text{Sn}_{0.16}$  MQW TL is important for present-day mid-infrared applications.

It is now interesting to investigate TE and TM optical gain spectra with the variation of photon energy. TE and TM optical gain spectra obtained in

Table V. Comparative study of the InGaAs and GeSn TL for modulation bandwidth

Multiple quantum well				Single quantum well			
GeSn TL BW (proposed structure)		InGaAs TL BW (theoretical) <sup>30</sup>		InGaAs TL BW (theoretical) <sup>31</sup>		InGaAs TL BW (experimental) <sup>36</sup>	
$t_{\text{qw}}$ (nm)	$I_{\text{bth}}/\text{BW}$	$t_{\text{qw}}$ (nm)	$I_{\text{bth}}/\text{BW}$	$t_{\text{qw}}$ (nm)	$I_{\text{bth}}/\text{BW}$	$t_{\text{qw}}$ (nm)	$I_{\text{bth}}/\text{BW}$
16	2.65 mA 52.29 GHz	16	7.08 mA 29 GHz	16	21.5 mA 21 GHz	16	23 mA 13.5 GHz

Analysis of a Direct-Bandgap GeSn-Based MQW Transistor Laser for Mid-Infrared Applications

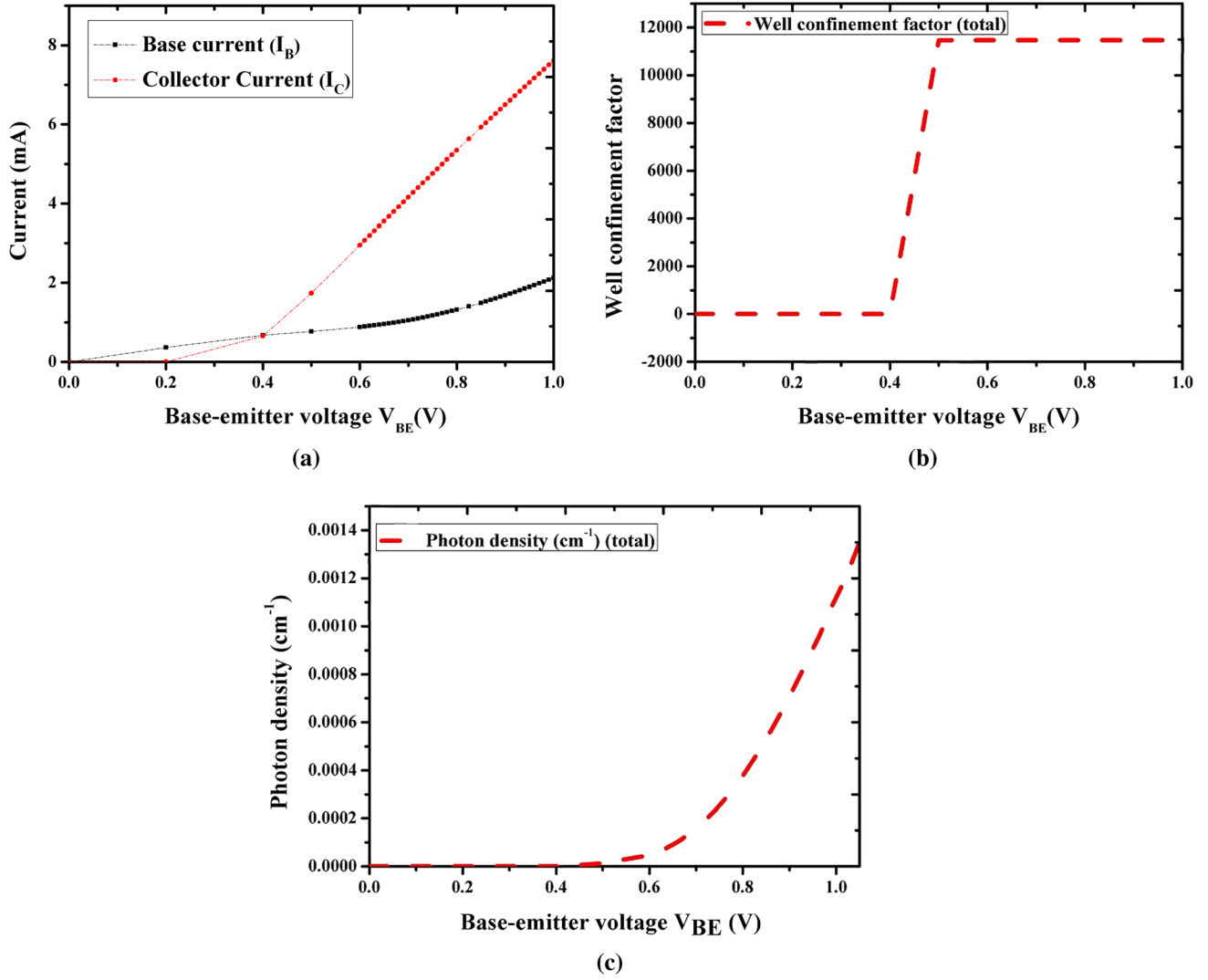


Fig. 6. (a) illustrates base current and collector current with the variation of applied base-emitter voltage for (GeSn/SiGeSn) multiple quantum well (MQW) TL. (b) Confinement factor across the wells at base-emitter voltage = 0.4 V ( $V_C = 2$  V, Sn = 16%, base doping concentration of  $1 \times 10^{18} \text{ cm}^{-3}$ ). (c) Photon density at base-emitter voltage = 0.4 V ( $V_C = 2$  V, Sn = 16%, base doping concentration of  $1 \times 10^{18} \text{ cm}^{-3}$ ).

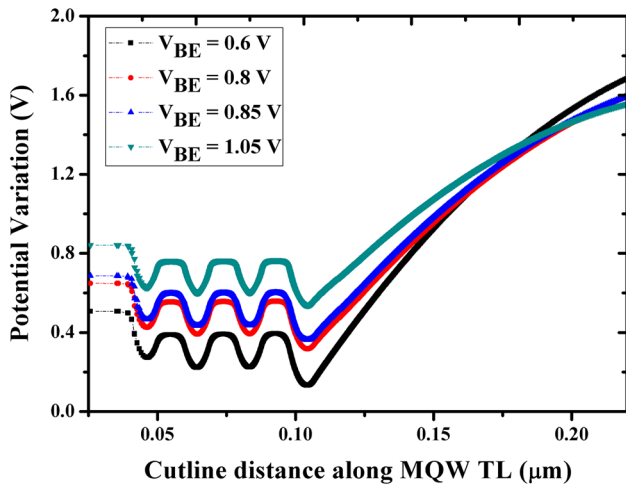


Fig. 7. Electric potential variation at different base-emitter voltages ( $V_{BE}$ ) (for  $V_C = 2$  V, Sn = 16%, base doping concentration of  $1 \times 10^{18} \text{ cm}^{-3}$ ).

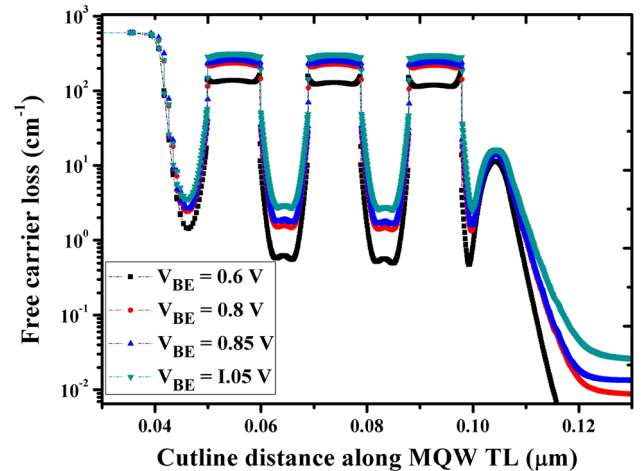


Fig. 8. Free carrier loss at different base-emitter voltages ( $V_{BE}$ ) (for  $V_C = 2$  V, Sn = 16%, doping concentration (base) of  $1 \times 10^{18} \text{ cm}^{-3}$ ).

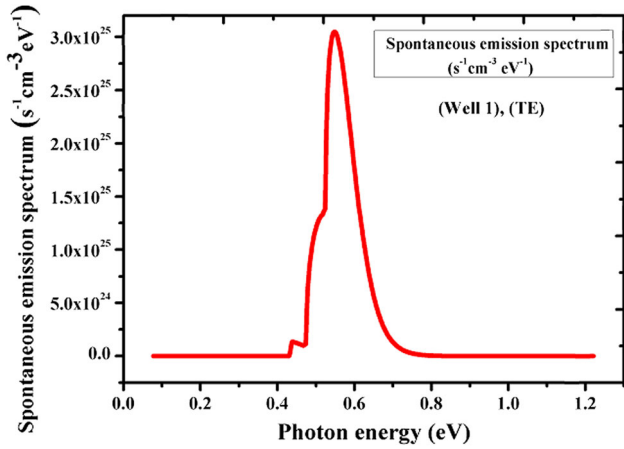


Fig. 9. Spontaneous emission with the variation of photon energy (for  $V_C = 2$  V, Sn = 16%, doping concentration (base) of  $1 \times 10^{18}$  cm $^{-3}$ ).

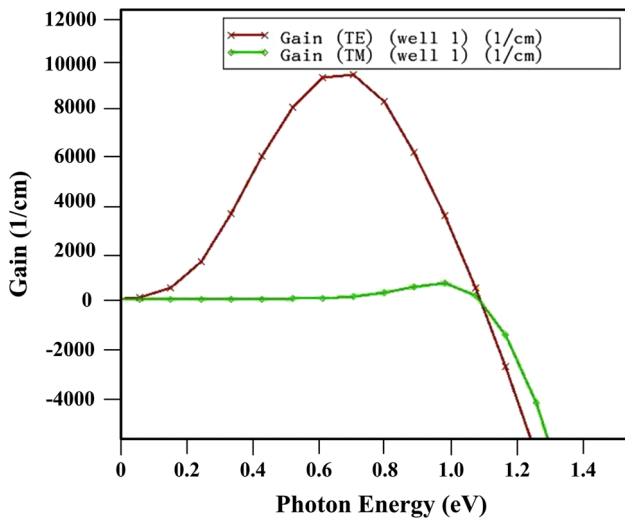


Fig. 10. Gain as a function of photon energy (for  $V_C = 2$  V, Sn = 16%, doping concentration (base) of  $1 \times 10^{18}$  cm $^{-3}$ ).

the QW (active region) of the GeSn TL structure is shown in Fig. 10. Since the heavy hole (HH1) transition has a dominant momentum matrix element (TE), the TE optical gain is significantly larger in contrast to the TM optical gain in this MQW TL. In addition, due to the lighter effective mass of heavy hole, there is a sudden rise in TE gain reaching the lasing threshold condition. Also, with the introduction of compressive strain in the GeSn wells, the top valence band behave as a heavy hole (HH) band, giving dominant TE gain in this TL. The peak of the TE optical gain spectra is around 0.63 eV, corresponding to an emission wavelength of 2.883  $\mu$ m. Thus, results ensure that GeSn based TL is suitable for a wide range of applications in the mid-infrared region.

Figure 11a illustrates the optical intensity across the base region of multiple quantum well TL. The maximum value of optical intensity is achieved in the middle of the base region and starts decreasing as we move outwards from the middle portion of the base region. It ensures that stimulated emission takes place in the QW regions and enables coherent emission of light for mid-infrared range once the base current reaches its threshold value. Figure 11b shows the plot at different base-emitter voltages ( $V_{BE}$ ) (for  $V_C = 2$  V, Sn = 16%, base doping concentration of  $(1 \times 10^{18}$  cm $^{-3}$ ). As vertical cutline is applied through the base region of GeSn TL structure, it is now interesting to show that how the optical intensity increases in the active region of GeSn based TL as we increase the base-emitter voltage from 0.6 V to 1.05 V.

Figure 12 shows the radiative recombination rate ( $R_{Rad}$ ) at different base-emitter voltages ( $V_{BE}$ ) (for  $V_C = 2$  V, Sn = 16%, base doping concentration of  $1 \times 10^{18}$  cm $^{-3}$ ). Carriers escaping from the emitter terminal have to travel the barrier and recombination takes place. This recombination leads to non-radiative recombination resulting in spontaneous

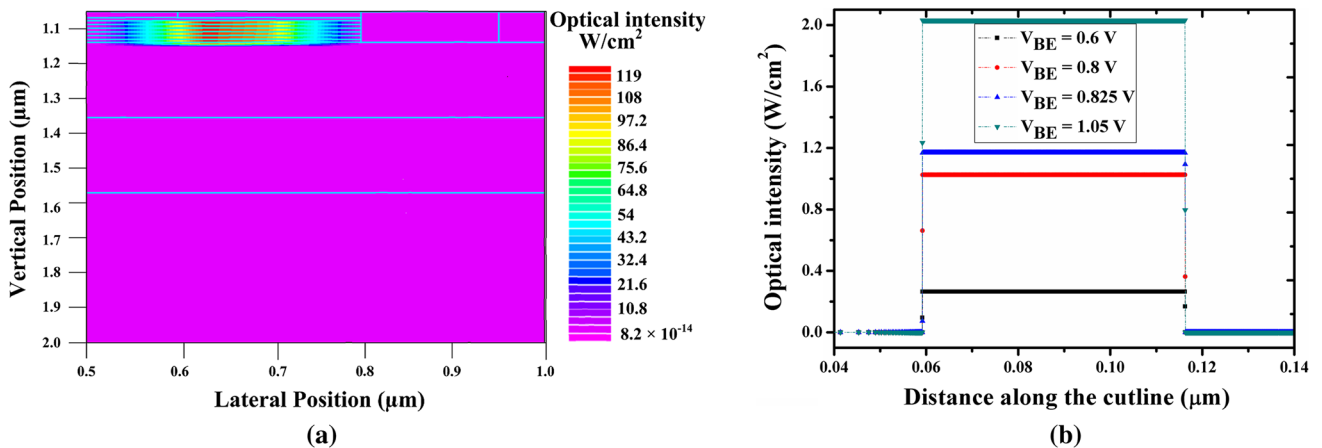


Fig. 11. (a) Cross-sectional view of the optical intensity and (b) its cutline plot at different base-emitter voltages ( $V_{BE}$ ) (for  $V_C = 2$  V, Sn = 16%, doping concentration (base) of  $1 \times 10^{18}$  cm $^{-3}$ ).

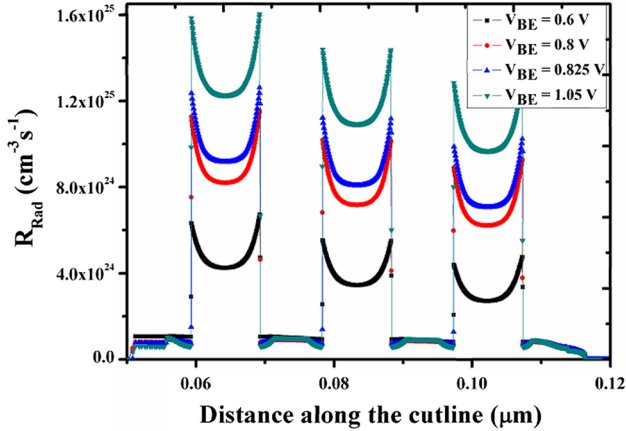


Fig. 12. Radiative recombination rate ( $R_{\text{Rad}}$ ) at different base-emitter voltages ( $V_{\text{BE}}$ ) (for  $V_{\text{C}} = 2$  V, Sn = 16%, doping concentration (base) of  $1 \times 10^{18} \text{ cm}^{-3}$ ).

operation, so this recombination must be reduced. Carriers confined in QWs will only lead to the lasing operation. Therefore, carriers should travel less in the barrier and, furthermore, they should remain in quantum wells. From Fig. 12, it is clearly seen that the carriers trapped in quantum wells contribute to the radiative recombination process and ensure the lasing operation for mid-infrared applications. Remaining carriers go to the collector region, which leads to electrical output. In addition, an increase in the base-emitter voltage of the GeSn TL owing to more carrier recombination in the quantum well regions and contributing to coherent light emission.

## CONCLUSION

In this work, we have studied, both analytically and using simulation, the performance of GeSn-based MQW TL. We have estimated the terminal currents, threshold base current, light output power, and modulation BW of a TL having GeSn/SiGeSn MQW in the base. We have also studied the effect of varying quantum well width on the threshold base current. In addition, various simulated characteristics such as potential variation, free carrier loss, confinement factor, spontaneous emission rate density, and radiative recombination rate have also been studied. The results show that light output power is strongly dependent on the base current, and the width of the quantum well significantly influences the threshold base current. The estimated results show that the lower value of threshold base current  $\sim 2.65$  mA and the modulation BW of  $\sim 53$  GHz have been predicted. Having the CMOS compatibility, high modulation bandwidth, and lower threshold base current, we conclude that the proposed GeSn-based TL can be used as high-performance laser for a wide range of applications at a mid-infrared wavelength of  $2.883 \mu\text{m}$  such as gas-sensing, chemical process monitoring, and molecular spectroscopy.

## ACKNOWLEDGEMENTS

Jaspinder Kaur would like to thank MHRD (India), for providing financial support in the form of Junior Research Fellowship (JRF). All of the authors are thankful to Professor Praveen Kumar, Director, NIT Delhi, for his encouragement and support to undertake this work.

## REFERENCES

1. N. Holonyak and M. Feng, *IEEE Spectr.* 43, 50 (2006).
2. H.W. Then, M. Feng, and N. Holonyak, *Proc. IEEE* 101, 2271 (2013).
3. M. Feng, N. Holonyak, B. Chu-Kung, G. Walter, and R. Chan, *Appl. Phys. Lett.* 84, 4792 (2004).
4. R. Basu, B. Mukhopadhyay, and P.K. Basu, *Semicond. Sci. Technol.* 26, 105014 (2011).
5. I. Taghavi, H. Kaatuzian, and J.P. Leburton, *Integrated photonics research, silicon and nanophotonics*, p. 5 (2012).
6. P.K. Basu, B. Mukhopadhyay, and R. Basu, *IET Optoelectron.* 7, 71 (2013).
7. O. Esame, Y. Gurbuz, I. Tekin, and A. Bozkurt, *Microelectron. J.* 35, 901 (2004).
8. P.K. Basu, B. Mukhopadhyay, and R. Basu, *Semiconductor Laser Theory* (CRC Press, Boca Raton, 2015).
9. S. Zaima, O. Nakatsuka, T. Asano, T. Yamaha, S. Ike, A. Suzuki, K. Takahashi, Y. Nagae, M. Kurosawa, W. Takeuchi, Y. Shimura, and M. Sakashita, in *2016 IEEE Photonics Society Summer Topical Meeting Series, SUM 2016*, p. 37 (2016).
10. V. Chakraborty, S. Dey, R. Basu, B. Mukhopadhyay, and P.K. Basu, *Opt. Quantum Electron.* 49, 1 (2017).
11. P. Moontragoon, R.A. Soref, and Z. Ikonc, *J. Appl. Phys.* 112, 073106 (2012).
12. H. Kumar and R. Basu, *IEEE Sens. J.* 18, 9180 (2018).
13. S. Wirths, R. Geiger, N. Von Den Driesch, G. Mussler, T. Stoica, S. Mantl, Z. Ikonc, M. Luysberg, S. Chiussi, J.M. Hartmann, and H. Sigg, *Nat. Photonics*, 9, 88 (2015).
14. B. Dutt, S. Member, H. Lin, D.S. Sukhdeo, S. Member, B.M. Vulovic, S. Gupta, D. Nam, S. Member, K.C. Saraswat, and J.S.H. Jr, *IEEE J. Sel. Top. Quantum Electron.* 19, 1502706 (2013).
15. M. Ohme and E. Al, *Appl. Phys.* 101, 2 (2012).
16. B.-J. Huang, J.-H. Lin, H.H. Cheng, and G.-E. Chang, *Opt. Lett.* 43, 1215 (2018).
17. R. Basu, V. Chakraborty, B. Mukhopadhyay, and P.K. Basu, *Opt. Quantum Electron.* 47, 387 (2015).
18. G. Chang, R. Basu, and B. Mukhopadhyay, *IEEE J. Sel. Top. Quantum Electron.* 22, 425 (2016).
19. A.K. Pandey, R. Basu, and G.E. Chang, *IEEE Sens. J.* 18, 5842 (2018).
20. G.-E. Chang, S.-W. Chang, and S.L. Chuang, *IEEE J. Quantum Electron.* 46, 1813 (2010).
21. R. Ranjan and M.K. Das, *Opt. Quantum Electron.* 48, 1 (2016).
22. S.W. Chang and S.L. Chuang, *IEEE J. Quantum Electron.* 43, 249 (2007).
23. P. Moontragoon, Z. Ikonc, and P. Harrison, *Semicond. Sci. Technol.* 22, 742 (2007).
24. G.-E. Chang, S.-W. Chang, and S.L. Chuang, *Opt. Express* 17, 11246 (2009).
25. M. Giehler, H. Kostial, R. Hey, and H.T. Grahn, *J. Appl. Phys.* 96, 4755 (2004).
26. J.I. Pankove, *Phys. Rev. Lett.* 4, 454 (1960).
27. J.I. Pankove, *Prog. Semicond.* 9, 48 (1965).
28. Silvaco, ATLAS User's Manual, Silvaco International, Santa Clara, CA, vol. 1 and 2, p. 1 (2015).
29. B. Faraji, W. Shi, D.L. Pulfrey, and L. Chrostowski, *IEEE J. Sel. Top. Quantum Electron.* 15, 3 (2009).
30. N. Kumar, B. Mukhopadhyay, and R. Basu, *Opt. Quantum Electron.* 50, 1 (2018).

31. R. Basu, B. Mukhopadhyay, and P.K. Basu, *IEEE Photonics J.* 4, 1571 (2012).
32. R. Basu, B. Mukhopadhyay, and P.K. Basu, *Semicond. Sci. Technol.* 27, 015022 (2012).
33. R. Basu, B. Mukhopadhyay, and P.K. Basu, *J. Appl. Phys.* 111, 083103 (2012).
34. M. Feng, N. Holonyak, H.W. Then, and G. Walter, *Appl. Phys. Lett.* 91, 10 (2007).
35. H.W. Then, M. Feng, and N. Holonyak, *J. Appl. Phys.* 107, 094509 (2010).
36. M. Feng, N. Holonyak, A. James, K. Cimino, G. Walter, and R. Chan, *Appl. Phys. Lett.* 89, 1 (2006).
37. I. Taghavi, H. Kaatuzian, and J.P. Leburton, *Appl. Phys. Lett.* 100, 231114 (2012).

**Publisher's Note** Springer Nature remains neutral with regard to jurisdictional claims in published maps and institutional affiliations.